Space-charge effects in Penning ion traps

CrossMark

T. Porobić [a,*], M. Beck [e], M. Breitenfeldt [a], C. Couratin [c,1], P. Finlay [a], A. Knecht [a,b,2], X. Fabian [c], P. Friedag [e], X. Fléchard [c], E. Liénard [c], G. Ban [c], D. Zákoucký [d], G. Soti [a], S. Van Gorp [a,3], Ch. Weinheimer [e], E. Wursten [a], N. Severijns [a]

[a] KU Leuven, Instituut voor Kern- en Stralingsfysica, Celestijnenlaan 200D, 3001 Leuven, Belgium
[b] PH Department, CERN, CH-1211 Geneva 23, Switzerland
[c] LPC Caen, ENSICAEN, Universit de Caen, CNRS/IN2P3, F-14070 Caen, France
[d] Nuclear Physics Institute, ASCR, 250 68 Rež, Czech Republic
[e] Universität Münster, Institut für Kernphysik, Wilhelm-Klemm-Strasse 9, D-48149 Münster, Germany

ABSTRACT

The influence of space-charge on ion cyclotron resonances and magnetron eigenfrequency in a gas-filled Penning ion trap has been investigated. Off-line measurements with $^{39}K^+$ using the cooling trap of the WITCH retardation spectrometer-based setup at ISOLDE/CERN were performed. Experimental ion cyclotron resonances were compared with ab initio Coulomb simulations and found to be in agreement. As an important systematic effect of the WITCH experiment, the magnetron eigenfrequency of the ion cloud was studied under increasing space-charge conditions. Finally, the helium buffer gas pressure in the Penning trap was determined by comparing experimental cooling rates with simulations.

© 2015 CERN for the benefit of the Authors. Published by Elsevier B.V. This is an open access article under the CC BY license (http://creativecommons.org/licenses/by/4.0/).

1. Introduction

In recent years, Penning ion traps have become established as versatile tools for trapping charged particles in plasma physics, atomic physics, as well as nuclear and particle physics. Specific applications include e.g. beam preparation [1], mass spectrometry [2], nuclear decay studies [3], antimatter studies [4], strongly coupled plasmas [5] and low energy precision measurements of fundamental interactions [6].

The Weak Interaction Trap for CHarged particles (WITCH) [7,8], the focus of this work, is a double Penning trap system situated at ISOLDE/CERN and aiming at determining the β–ν angular correlation coefficient a in the mirror β-decay of ^{35}Ar to a precision better than 0.5%. In the standard model, nuclear β-decay is modelled as a purely V (vector)–A (axial-vector) interaction. However, Lorentz invariance also allows scalar, tensor and pseudo scalar interaction components. At present, the existence of scalar and tensor currents is experimentally ruled out to a precision of only about 10% [9]. The β–ν angular correlation coefficient's sensitivity to the exotic scalar current in the case of ^{35}Ar in principle allows providing stringent experimental constraints on physics beyond the standard model [8,6,10,11].

The WITCH Penning traps act as a scattering-free source of radioactive ^{35}Ar, typically containing large ion clouds (with 10^4–10^6 ions) to enhance statistics. However, if more than one ion is present in a Penning trap, the trapping potential deviates from the quadrupolar shape and causes shifting of motional eigenfrequencies, as well as shifting and widening of the ion cyclotron resonance frequency required for sideband cooling [1,12]. Moreover, centering becomes more difficult due to Coulomb repulsion. Consequently, this hampers efficient ion cloud cooling, centering and purification. Space-charge thus significantly contributes to systematic effects caused by source properties, i.e. ion cloud dimensions and temperature. Ion clouds of this size and density are still not fully in the plasma régime, and are therefore beyond reach of both single particle and collective motion analytical frameworks. Numerical simulation presently remains the only feasible way of modelling such phenomena. For this purpose, the Simbuca [13] simulation package was employed in this work on graphical processor units (GPUs), taking advantage of their intrinsic parallelism.

* Corresponding author.
E-mail address: tomica.porobic@fys.kuleuven.be (T. Porobić).
[1] Present address: KU Leuven, Instituut voor Kern- en Stralingsfysica, Celestijnenlaan 200D, 3001 Leuven, Belgium.
[2] Present address: Paul Scherrer Institut, 5232 Villigen PSI, Switzerland.
[3] Present address: Atomic Physics Laboratory, RIKEN, Saitama 351-0198, Japan.

Many other Penning trap experiments experience limitations caused by space charge-related effects. ISOLTRAP's precision mass spectrometry depends on precise determination of the ions' fast eigenmotion frequency and efficient isobar purification at the MR-ToF device [14], both being affected by frequency shifts and other space-charge phenomena [15]. REXTRAP [16], a high-capacity preparation trap at ISOLDE, aims for mass-selective operation, as well as efficient cooling of large (10^8) ion clouds. PIPERADE [17] (currently under construction) is a high-capacity isobar separator for the SPIRAL2/DESIR facility, the operation of it being limited by a space-charge induced frequency broadening and shift of the sideband cooling frequency.

In the case of WITCH, understanding of such phenomena is essential not only for efficient tuning and operation of the traps, but also for an accurate characterization of the systematic effects observed in on-line experiments. Furthermore, successful numerical simulation is important for gaining a deeper understanding of space-charge effects in current Penning trap experiments, as well as for the design of future ones. In this work, a systematic experimental and computational study of space-charge effects on ion motional modes and buffer-gas cooling efficiency is presented, thereby extending earlier work that was reported in [18,1,19,13].

2. Nonneutral plasma in a Penning trap

2.1. Penning trap principles

Charged particles are axially confined in a Penning trap by a strong axial magnetic field $\mathbf{B} = B\hat{\mathbf{e}}_z$ and radially by an electrostatic quadrupolar potential of the form

$$U = \frac{U_0}{2d^2}(z^2 - r^2/2) \tag{1}$$

where U_0 is the potential between the end cap and ring electrodes, and d is a parameter given by the trap geometry, characterizing the depth of the potential well.

The motion of a single particle is then a superposition of three eigenmotions with corresponding eigenfrequencies: the magnetron (ω_-), the axial harmonic (ω_z), and the modified cyclotron (ω_+) motion. The radial frequencies satisfy equation

$$\omega_\pm = \frac{\omega_c}{2} \pm \sqrt{\frac{\omega_c^2}{2} - \frac{\omega_z^2}{2}} \tag{2}$$

while the axial frequency is given by

$$\omega_z = \sqrt{\frac{qU_0}{md^2}} \tag{3}$$

where q and m are the charge and mass of the ion. The sum of the two radial frequencies is the true cyclotron frequency (ω_c), given by

$$\omega_c = \omega_+ + \omega_- = \frac{q}{m}B. \tag{4}$$

For high magnetic fields the three eigenfrequencies satisfy the following inequality: $\omega_- \ll \omega_z \ll \omega_+$.

After entering the trap, ions start losing their kinetic energy via collisions with the buffer gas. This interaction can be modelled phenomenologically by a continuous drag force acting in the direction opposite to the ions' motion

$$\mathbf{F} = -\delta m\mathbf{v} \tag{5}$$

where δ is the damping constant, given by

$$\delta = \frac{q}{K_{mob}} \frac{p/p_N}{T/T_N} \tag{6}$$

with K_{mob} being the reduced ion mobility, and p/p_N and T/T_N the gas pressure and temperature relative to normal pressure and temperature, respectively. In this model, the axial harmonic oscillation and reduced cyclotron radial motion amplitude (R_+) are damped, while the magnetron motion is unstable, and its amplitude (R_-) increases as

$$R(t) = R_\pm(0)e^{(\mp\delta(\omega_\pm/(\omega_- + \omega_+))t)}. \tag{7}$$

This effect can be mitigated by coupling the magnetron motion to either the axial or the reduced cyclotron motions via radio-frequency (RF) excitations at the sum of frequencies of both motions. The latter coupling is usually used with ions, with the RF frequency $\omega_{rf} = \omega_c = \omega_+ + \omega_- = \omega_{cool}$ in the case of a single ion, where ω_{cool} represents the *optimal* centering and cooling frequency of the RF excitation, i.e. the frequency for which the highest number of ions is centered. In this way, the radius of the magnetron motion can be decreased, resulting in centering and cooling of the trapped ions. This method, known as buffer gas (or sideband) cooling [20], is used by many Penning trap systems for ion cooling and centering, e.g. REXTRAP, ISOLTRAP [21] and SHIP-TRAP [22]. Because of its mass selectivity, it is also used for ion species purification when magnetic beam separator resolution is not sufficient.

With only one ion in the trap, the equations of motion can be solved analytically, with both the buffer gas and the excitation field taken into account, resulting in damped oscillatory inter-conversion of the fast and slow radial motions

$$R(t) = R_\pm(0)e^{(-\delta/2t)}. \tag{8}$$

This cooling and centering continues until thermal equilibrium with the buffer gas is reached, limiting the final amplitudes.

2.2. Many ions in a Penning trap

When more than one ion are present in a Penning trap, the increased space-charge modifies the net potential influencing the ions, and the observed effects start to diverge from the single-particle theory outlined in the previous subsection, making the problem difficult to approach analytically. The space charge produced by $\sim 10^5 - 10^7$ ions typically present in a high-capacity trap like WITCH causes significant deviations from the single-particle picture, but still does not always satisfy the criterion for a true plasma, i.e. the Debye length $\lambda_D = \sqrt{kT/4\pi\rho^2}$, where T and ρ are respectively the temperature and the density, can still exceed the cloud's dimensions. Consequently, numerical simulation is the only feasible approach for ion cloud dynamics modelling in these cases. Nevertheless, many plasma physics results remain valid in this intermediate region [23].

An ion cloud of a prolate spheroidal form and constant density in the center of a Penning trap will produce a radially outward electric field proportional to r, the radius. This field causes the $\mathbf{E} \times \mathbf{B}$ drift, resulting in a rigid rotation of the cloud around its main axis, i.e. the fourth eigenmotion at the frequency

$$\omega_r = \frac{a(\alpha)\rho q}{\epsilon_0 B} \tag{9}$$

where a is a coefficient determined by the spheroid aspect ratio α, ρ is the ion cloud density and ϵ_0 is the dielectric constant. Since the frequency ω_{cool} is given in the reference frame of the ion cloud, the rotation causes an increase of the sideband cooling frequency in the laboratory frame, ω'_{cool}. This shift amounts to $2\omega_r$ in the ideal case [1], but if the density of the cloud is not constant, making its potential no longer quadratic, the problem becomes approachable only via numerical simulation. Through modifying the effective potential in the trap, the space-charge also changes
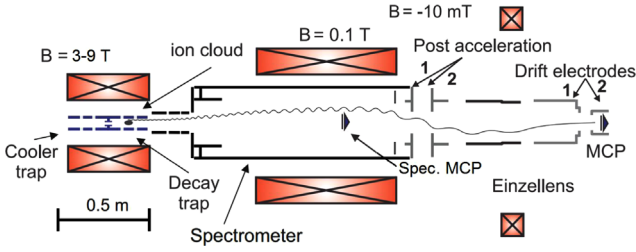
Fig. 1. Schematic overview of the WITCH Penning traps with the retardation spectrometer, spectrometer MCP, re-acceleration section and position-sensitive MCP.

Fig. 2. Schematic overview of the WITCH Penning traps with their electrodes marked (C stands for cooler trap, and D for decay trap). The pumping diaphragm between the traps is not shown. High voltage is applied on the end cap electrodes while ions still have high energy. A quadrupolar trapping potential around the trap center (CRE and DRE electrodes) is achieved with correction (CCE and DCE) and central ring electrodes. Ions are excited by a time dependent potential on the eightfold segmented central ring electrodes. Figure taken from [31].

the motional eigenfrequencies [24]

$$\omega'_\pm = \frac{\omega_c}{2} \pm \sqrt{\left(\frac{\omega_c}{2}\right)^2 - \frac{1}{2}\omega_z^2 - \frac{\omega_p^2}{3}} \tag{10}$$

where $\omega_p^2 = \rho q/m\epsilon_0$ is the plasma frequency. This results in a decrease of the modified cyclotron frequency ω_+ and an increase of the magnetron frequency ω_- with increasing space-charge. Eq. (10) is valid for spherical ion clouds with constant density. The denominator of the plasma frequency term stems from the cloud shape, and for prolate ellipsoids becomes smaller than 3 [25].

3. Experimental setup

In a radioactive beam experiment with the WITCH setup (see Fig. 1), cooled bunches of ^{35}Ar are prepared in REXTRAP and then sent into the WITCH beam line at 30 keV kinetic energy before being pulsed down to about 9 keV by a pulsed drift cavity [19]. They are further decelerated electrostatically to ~ 100 eV before entering the cooler trap (CT), where they are captured in a nested potential (a low quadrupolar potential around the trap center with high box-like potential on the end caps) and thermalized with the helium buffer gas (to ~ 0.025 eV), with a total efficiency of $\sim 20\%$. The cooled and centered ions are transferred to the second Penning trap (decay trap, DT) that serves as a scattering-free source. ^{35}Cl daughter ions recoil from the decay trap into a retardation spectrometer (MAC-E filter [26]), where their integral energy spectrum is probed by a variable retardation barrier. Since the DT is situated in a high magnetic field region (typically 3–9 T) and the analysis plane of the retardation spectrometer is in a low field region (0.1 T), up to 98.33% of the ions' radial energy is converted to axial energy. The ions that pass the retarding potential are re-accelerated by a 3 kV potential and focused on a position sensitive Micro-Channel Plate (MCP) detector [27,28].

All experiments presented in this work have been performed using stable ^{39}K$^+$ ions originating from REXTRAP's offline ion source and subsequently cooled and bunched by REXTRAP, or from WITCH's dedicated off-line surface ionization ion source with an RFQ for cooling and bunching [29].

3.1. WITCH Penning traps

The WITCH ion trapping system [7,30] consists of two cylindrical Penning traps (electrode layout shown in Fig. 2). The first (CT) is used for preparation of the ion cloud using buffer gas and excitations, while the second (DT) serves as storage for the ion cloud and acts as a scattering-free radioactive source. To achieve sufficient vacuum conditions for the radioactive source and spectrometer, the DT is separated from the CT, which contains He buffer gas at $10^{-5} - 10^{-4}$ mbar, by a differential pumping diaphragm of 2 mm diameter. They are both situated within a superconducting magnet with field homogeneity of $\delta B \leq 10^{-5}$.
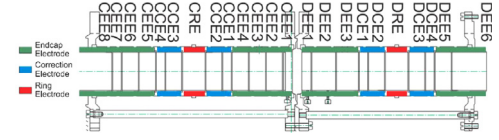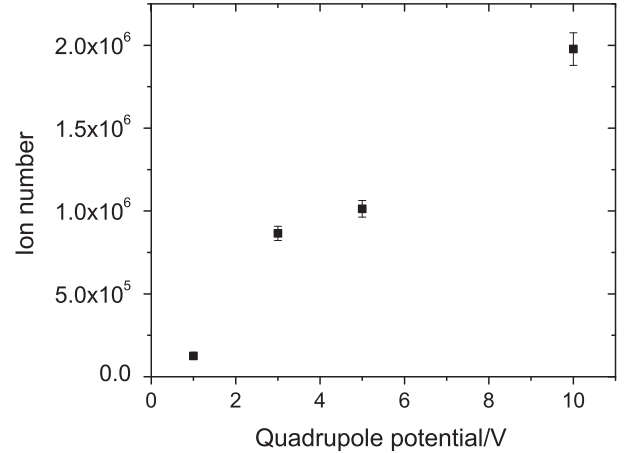

Fig. 3. The dependence of the trap capacity on the depth of the quadrupolar potential well after 300 ms of buffer gas cooling with quadrupolar excitations at 3 V amplitude.

The trap electrodes have a 4 cm diameter and are made of oxygen-free copper double-coated with Ni and Au. The CT is 25 cm, while the DT is 20 cm long. Each trap has an eight-fold segmented central electrode for creating the RF excitation potential. Their maximum ion capacity is estimated to $\sim 10^7$ ions, while the instantaneous capacity depends mainly on the space-charge of the ion cloud and the depth of the quadrupolar potential well in the trap, with typical operating values being in the range 0.5–15 V (see Fig. 3). The voltages on the electrodes between the end cap and the central electrode are scaled so as to produce a quadrupolar potential well in the region of a few centimeters around the trap center.

The detection system used for these measurements consisted of two MCP detectors (the first in front of the CT and the second one behind the DT, in the spectrometer), a Faraday cup (FC) situated in front of the traps on the same feedthrough as the first MCP, and a full range pressure gauge close to the buffer gas valve. Since this gauge is located outside the trap, it was used only for indirect estimation of the buffer gas pressure in the CT.

3.2. Measurement procedure

The number of ions entering the trap was controlled via beam line electrodes with a switch (beam gate) before the ions were pulsed down to low kinetic energies. As the pulsed-down ions approached the CT, its lower end cap electrode (CEE8 in Fig. 2) was set below 0 V, while the upper end cap (CEE1) was at a potential sufficient to block the ions (50–200 V, depending on the tuning, Fig. 4a). When the bunch was fully within the trap, CEE8 was raised to the same potential as CEE1 (Fig. 4b). This loading procedure was repeated several times if large ion clouds were needed.
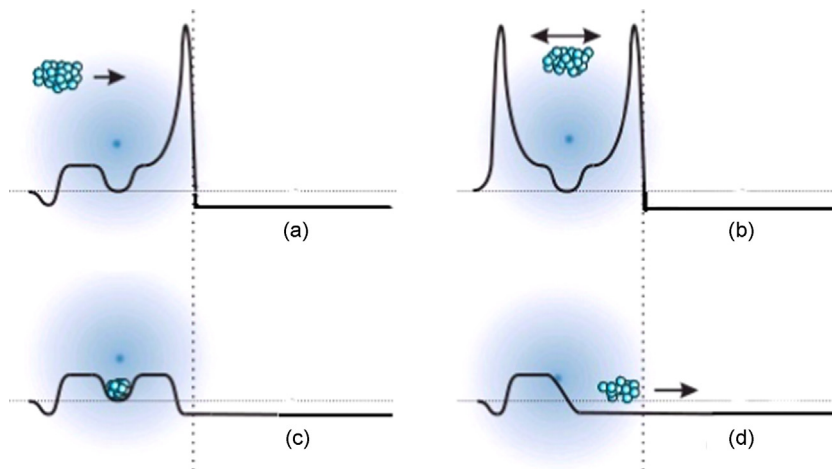
Fig. 4. Operation of the cooler Penning trap. (a) Ions entering the trap. (b) High (~ 100 eV) energy ions trapped by the end caps. (c) Ions cooled into a quadrupolar potential in the trap center, end caps potential lowered, excitations applied. (d) Cloud ejected from the CT towards the diagnostic MCP behind the traps.

When the ions had lost enough kinetic energy through buffer gas collisions, the end cap potentials were lowered and the ions were fully confined by the quadrupolar potential of the inner electrodes (Fig. 4c). Typically, this process takes up to 200 ms, depending on the buffer gas pressure. If needed, at this point a quadrupolar RF field could be applied to center and compress the ion cloud. For that purpose, the RF was applied at ω_{cool} and 3 V amplitude, for 20–120 ms.

Since radial compression via excitations can expand the cloud axially, a short cooling period without excitation to reduce axial amplitudes followed if needed. Finally, the ions were ejected through the pumping diaphragm and DT, both at 0 V (Fig. 4d), and were detected with the diagnostic MCP in the spectrometer. Cooling and centering efficiency for the particular measurement are given by the number of ions passing through the diaphragm and being detected on the MCP.

4. Experimental results

4.1. MCP calibration

For estimating the absolute number of ions in the Penning trap, a calibrated, chevron-stacked, 4 cm diameter MCP detector manufactured by Photonis was used. It was operated in integral mode, adding all the charge impinging on its surface into a single pulse. It was shown previously that the area of such a pulse can accurately represent the amount of charge impinging on the detector plates [28], provided special care is taken to avoid saturation effects. WITCH and REXTRAP's offline ion sources provided ^{39}K cooled ion bunches used for this calibration. The ion number per bunch was varied using an electrode synchronized with the measurement cycle as a beam gate. The MCP plates were biased to -2 kV and the signal height and the area were read out by an oscilloscope connected to a PC running a Labview based control and data acquisition system [32]. The MCP was calibrated in situ, without breaking the vacuum between the calibration and subsequent measurements. The calibration was performed using a Keithley 6514 electrometer connected to a movable Faraday cup situated at the same axial position in the beam line as the MCP. Care was taken that both measuring devices capture the entire beam profile. Faraday cup current readings for each beam gate setting were averaged and recorded, together with MCP pulse heights and areas. The pulse heights were found to follow a linear dependence with the pulse areas and the charge measured by the Faraday cup, as shown in Fig. 5. This allowed using both the pulse areas and
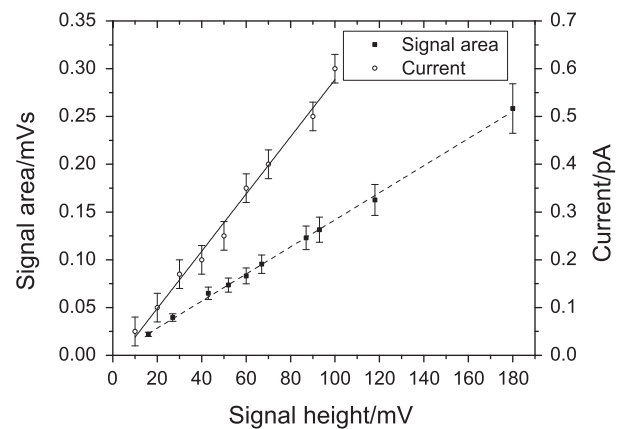

Fig. 5. (Right axis) Averaged ion beam current, measured with an electrometer connected to a Faraday cup, showing a linear dependence with the height of the signal on the MCP, validating the MCP calibration for ion bunches resulting in averaged currents below 0.6 pA. (Left axis) Area of the MCP signal, showing a linear dependence with the height of the signal on the MCP. Each data point represents an average of 10 measurements.

heights of the calibrated MCP to estimate the true number of ions in the Penning trap.

4.2. Effects of space-charge on cooling and centering

Like some other existing or planned Penning traps [1,17], WITCH operates under high space-charge conditions, leading to unwanted phenomena such as a shift and peak broadening of the cyclotron cooling resonance. Earlier investigations have already identified the relevance of these limiting factors for effective Penning trap operation [18,1,12,15]. In the case of a single ion species, it was found that both increased space-charge and increased buffer gas pressure lead to higher optimal cyclotron cooling and centering frequencies ω_{cool}, i.e. the frequencies corresponding to the peak of the RF excitation resonance.

In this section, systematic effects of space-charge and buffer gas pressure on the sideband cooling frequency ω_{cool} were studied. Ion clouds were prepared as described in Section 3.2 and ejected through the 2 mm diaphragm, with optimal cooling and centering resulting in greater intensities recorded on the diagnostic MCP.

Fig. 6 shows two series of measurements at different buffer gas pressures. The cyclotron resonance peak position and FWHM were measured for each, in dependence with the ion number. The preparation scheme consisted of 200 ms buffer gas cooling
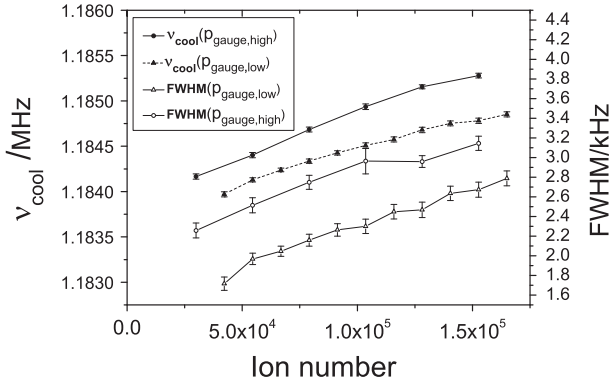
Fig. 6. Cyclotron frequency $\nu_{cool} = \omega_{cool}/2\pi$ and FWHM dependence on the number of ions and buffer gas conditions. Results are shown for two buffer gas pressures, i.e. $p_{gauge,low} = 0.8 \times 10^{-2}$ mbar and $p_{gauge,high} = 3.2 \times 10^{-2}$ mbar, measured outside the traps. The measurement sequence consisted of 200 ms cooling w/o excitations, 80 ms cooling and centering with quadrupolar excitation at 3 V, and ejection. The buffer gas pressure (p_{gauge}) was kept constant for each of the two measurements.
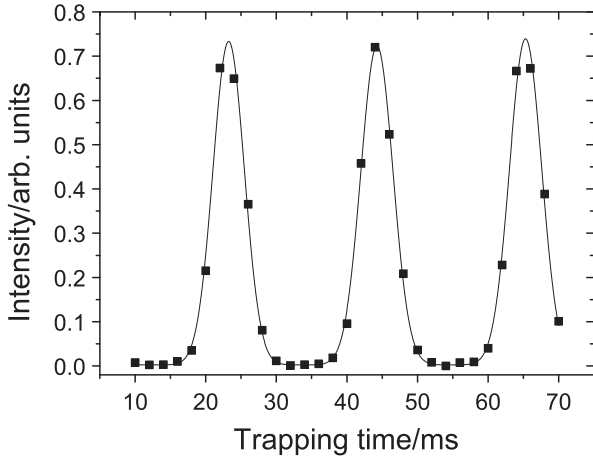

Fig. 7. Ion intensity measured after ejection of the ion cloud through the diaphragm. Because of the eccentricity of the magnetron motion, only certain phases result in full transmission through the diaphragm. A Gaussian function is fitted to each peak.

without excitations followed by 80 ms of quadrupolar RF cooling with 3 V amplitude. The buffer gas pressure, as measured with the gauge outside the traps, differed by a factor of four between the different measurements ($p_{gauge,low} = 0.8 \times 10^{-2}$ mbar, $p_{gauge,high} = 3.2 \times 10^{-2}$ mbar). In comparison with the estimation from Section 5.3, the pressures used here were lower and higher than the calibration point. However, the exact pressure in the cooler trap p_{CT} is difficult to estimate accurately, since its dependence on p_{gauge} is not known. With other experimental conditions unchanged, increased buffer gas pressure causes the resonance peak position to shift and FWHM to increase by a few hundred Hz in the high buffer gas case. Thus, while improving the cooling speed via collisions, too high buffer gas pressure hampers efficient centering and possible mass selective operation of the trap through resonance broadening. Peak positions and FWHMs are found to shift to higher values linearly with the number of ions, having roughly the same respective slopes for both buffer gas pressures.

Results shown here are only a subset of all results obtained in this experimental campaign. In others, different cooling and excitation schemes were used. The buffer gas cooling time was varied between 100 ms and 200 ms, and the excitation time in the 20–120 ms range, while p_{gauge} was typically varied in the range

given above. For all experimental conditions, the resonances were qualitatively similar to Fig. 6, i.e. there was a single Gaussian shaped resonance peak with properties consistently following the same trends with variable number of ions and buffer gas pressure. This consistency and reproducibility allowed us to compare the ion cloud behavior shown here to simulations, with the goal of optimizing operational trap parameters, benchmarking the Simbuca simulation software and providing insight into experimentally unavailable ion cloud properties (see Section 5).

4.3. Effects of space-charge on the magnetron motion

In a perfectly cylindrical Penning trap with a quadrupolar electrostatic potential, a centrally injected ion cloud (or one recentered by excitation) remains centered while the ions in it perform a magnetron motion around the trap's geometrical center. However, if the electrostatic field contains asymmetrical components, or if the geometric and magnetic field axes are not aligned, the center of the ion cloud will rotate around a point off the trap center at the magnetron frequency. This behavior was observed in the WITCH traps only for very low trap depths (~ 1 V).

In this case, an eccentric motion of the ion cloud in a shallow trap typically has a larger radius than the diaphragm situated between the CT and DT. Depending on the phase of the motion, this can result in the diaphragm blocking the ions upon ejection. This then causes a periodic dependence of ion intensity on trapping time, as shown in Fig. 7, with the difference between the peak central values corresponding to the magnetron motion period. This effect was further confirmed by ejecting the ion cloud from the traps onto a position sensitive MCP at different phases of the magnetron motion. From the radius of the motion projected on the detector, using the ion tracking simulation software SimWITCH [33], it was found that the radius of the ion cloud motion around the trap center ranges from 1 to 4 mm. This is still too far from the trap walls (electrodes have a diameter of 40 mm) to induce image charges large enough to significantly modify the magnetron frequency [24]. In the first approximation, the magnetron frequency of a single ion in the trap is given by Eq. (2). However, in high space-charge conditions, the additional radial electric field will shift this frequency to higher values, given by Eq. (10).

The effect of the eccentric motion of the ion cloud is found to be more pronounced for lower trapping potentials and disappears for higher ones (~ 15 V), since in the latter case the ion cloud is much more compact, resulting in larger numbers of ions successfully passing the diaphragm. Depending on the orientation of the crystal lattice at the surface, electrodes can have different contact potentials, i.e. a gold plated ring electrode, such as installed in both the CT and DT, can produce a potential difference of up to ~ 0.4 V [34] between its segments, causing a shift of the electrostatic trap center with respect to its geometric center. Together with a misalignment of the magnetic and electric fields, this effect was identified as a possible cause for the observed motion. A confirmation in the form of a direct measurement of the contact potential or the field misalignment is not available at this time. However, since the intensity of the radioactive source (ion cloud) is effectively modulated at the magnetron frequency as shown in Fig. 7, the characterization of ω_- and its space-charge dependence is essential for the analysis of the WITCH experiment online data.

Since the WITCH experiment, unlike other high space-charge traps, benefits from a low trapping potential to reduce other systematic effects [35], the eccentricity of the magnetron motion presents a significant systematic effect [36], introducing an oscillatory effect superposed on the retardation spectrum data. Furthermore, since each radioactive ion trap load varies due to target conditions and in-trap decay, any dependence of the magnetron frequency on the number of ions has to be
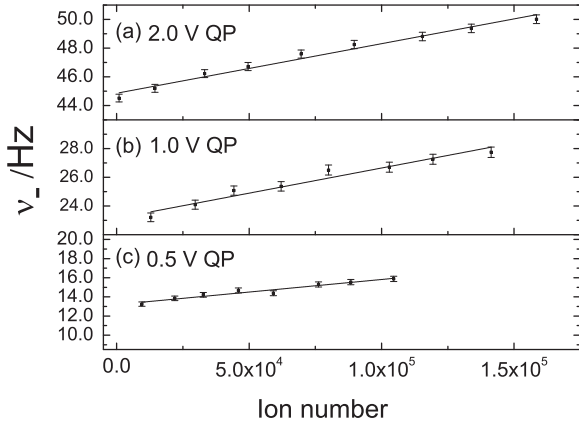
Fig. 8. Dependence of the experimental magnetron frequency, ν_-, on the number of ions for different quadrupolar trapping potential: (a) 2.0 V, (b) 1.0 V, and (c) 0.5 V.
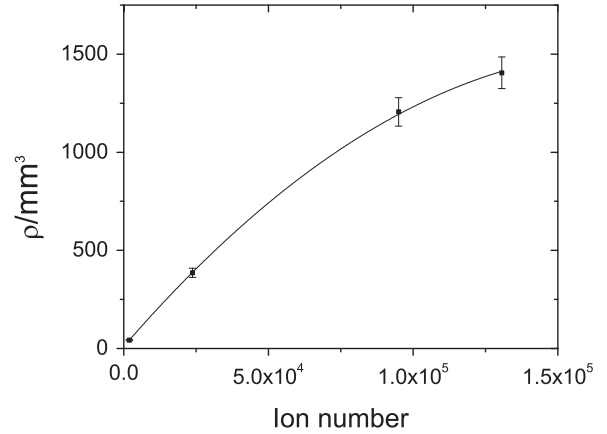

Fig. 9. Simulated average density of the ion cloud for different space-charge conditions. The density dependence is almost linear for ion numbers in the selected $10^4 - 10^5$ range. The volume of the cloud is defined as the volume containing 95% of all ions.

characterized and taken into account during data analysis. This effect was experimentally studied for different values of the trapping potential ranging from 0.5 V to 2 V and different amounts of charge in the trap (Fig. 8). It was found that the magnetron frequency increases linearly with the number of ions in the trap. Eq. (10) implies $\omega_- \propto \rho$ to first order, supposing that ρ is uniform. Since ρ is not experimentally available, it was simulated for the relevant space-charge range and other trap parameters matching the ω_- measurement. It was found that ρ varies significantly within the cloud, being highest in the center and very low at outer radii. An average ρ value was therefore calculated using the volume containing 95% of the ions. Its dependence on ion number was found to be approximately linear with a very small quadratic component, in the $10^4 - 10^5$ range (Fig. 9). Although the simulation confirms ρ is not uniform as is assumed in the theoretical calculation of the ω_- shift, the observed ω_- shift is still linear with ion number, suggesting that the exact shape of $\rho(r)$ does not have a large influence on the ω_- space-charge shift.

5. Simulations

Generally, the number of numerical operations needed for a Coulomb interaction simulation scales with $\mathcal{O}(N^2)$, where N is the number of particles, but approximative methods such as the Barnes–Hut tree [37] and fast multipole method [38] reduce this to $\mathcal{O}(N\log N)$ and $\mathcal{O}(N)$, respectively. Recently, a novel *ab initio* method for N-body gravitational interaction simulations using GPUs was developed [39] and implemented in Simbuca [13], a software package for simulation of trapped ion cloud dynamics. Simbuca implements the K_0 realistic buffer gas collision model [40] and dipolar, quadrupolar, octupolar and rotating wall excitations, together with customized electro- and magnetostatic field maps. The fifth-order Dormand–Prince [41] method with adaptive time step was used as an integrator. In the following, Simbuca simulations of the effect of space-charge on the cyclotron resonance frequency and FWHM will be presented and compared with experimental data.

5.1. Setup of the simulations

The effect of space-charge on the cyclotron resonance frequency, i. e. the frequency ν_{cool} at which the magnetron-cyclotron motion interconversion via quadrupolar excitation achieves maximal effectiveness, was investigated using the Simbuca simulation software by scanning the excitation frequency around ν_c. Simulation parameters were selected to reproduce the experimental conditions described in

Section 4.2. The magnetic field map was obtained from the manufacturer (Oxford Instruments), and the electrostatic field of the cylindrical electrode stack calculated using a COMSOL [42] model matching the trap geometry laid out in Section 3.1. The asymmetry of the CT potential described in Section 4.3 is not accounted for by the simulations, but does not play a role in the ν_{cool} scans presented here, as it does not cause a measurable effect for the high end cap potentials of ~ 15 V used in these measurements. Ion clouds of 500–2000 ions with their charge scaled to simulate space-charge conditions corresponding to clouds of $10^3 - 2 \times 10^5$ ions were simulated (the consistency of this approach is shown in Section 5.2).

The ions are created in the center of the trap within a prolate spheroid with a radius of 1–2 mm and major axis of 10–20 mm and are given an initial kinetic energy (KE), Gaussian distributed and centered around 50 eV. Furthermore, it was found that the initial KE has no influence on the cooling rate of the ion cloud, i.e. the average KE decays exponentially with a time constant determined only by the intrinsic buffer gas parameter δ, in agreement with buffer gas cooling theory (Eq. (8)).

5.2. Consistency of the Coulomb scaling

Implementation on a GPU allows for a large degree of parallelization in N-body interaction calculations and results in simulation times reduced by orders of magnitude compared to a modern CPU. While this provides a large improvement in computational speed, simulating ion clouds with N larger than a few thousand is still impractical with modern GPUs, and a scaled Coulomb method is therefore employed here. The linearity and consistency of this approximation was verified to hold up to a scaling factor (SF) of about 100.

The Coulomb scaling was tested by direct comparison of ion clouds scaled up to a factor of 6 to reference clouds of 1^+ ions, e.g. a cloud of 500 6^+ ions was compared to a cloud of 3000 1^+ ions. However, since it is not feasible to test the scaling factors directly for ion clouds larger than a few thousand ions due to computation time constraints, the simulations were set up so as to cross-check increasing scaling factors from 1 to 1024, for pairs of ion clouds scaled to the same total charge and ranging from 10^3 to 5×10^5 ions. Clouds of 1000 ions scaled by a factor of n and a cloud of 500 ions scaled by a factor of $2n$ were compared (see Table 1), with n ranging from 1 to 512.

The ion clouds were subjected to cooling and centering schemes matching the ones used in other simulations presented here, i.e. consisting of 200 ms cooling from a high (10–50 eV) kinetic energy, 80 ms of centering with quadrupolar excitations

Table 1

Number of simulated ions and their Coulomb scaling factor (SF), average radius (R), average axial displacement (Z) and average energy per ion (E) at $t=290$ ms. The error bars are the standard deviations of several values of R, Z and E around $t=290$ ms, the end of the cycle. Top 6 rows show a direct comparison of scaled ion clouds to a reference cloud with 1^+ ions, while the rest show a comparison of clouds of 500 ions scaled by $2n$ to clouds of 1000 ions scaled by n, with n increasing from 2 to 512. The dependence of the parameters on the scaled number of ions in the case of 1000 simulated ions is shown in Fig. 10.

Ions	SF	R/mm	Z/mm	E/eV
1000	1	0.490 ± 0.013	2.11 ± 0.04	3.08 ± 0.14
500	2	0.500 ± 0.009	2.12 ± 0.05	3.25 ± 0.16
2000	1	0.491 ± 0.011	2.05 ± 0.03	2.58 ± 0.15
500	4	0.503 ± 0.008	2.16 ± 0.08	2.81 ± 0.12
3000	1	0.494 ± 0.010	2.06 ± 0.05	2.26 ± 0.11
500	6	0.500 ± 0.009	2.11 ± 0.09	2.27 ± 0.09
1000	2	0.503 ± 0.014	2.10 ± 0.03	2.84 ± 0.19
500	4	0.503 ± 0.008	2.16 ± 0.08	2.81 ± 0.12
1000	4	0.494 ± 0.017	2.15 ± 0.05	2.15 ± 0.12
500	8	0.507 ± 0.009	2.07 ± 0.08	2.29 ± 0.11
1000	8	0.498 ± 0.008	2.24 ± 0.09	1.98 ± 0.09
500	16	0.501 ± 0.008	2.22 ± 0.03	1.94 ± 0.10
1000	16	0.516 ± 0.012	2.48 ± 0.03	1.94 ± 0.09
500	32	0.501 ± 0.008	2.22 ± 0.03	1.94 ± 0.10
1000	32	0.511 ± 0.008	2.79 ± 0.04	1.92 ± 0.10
500	64	0.500 ± 0.006	3.07 ± 0.08	1.94 ± 0.08
1000	64	0.497 ± 0.005	3.38 ± 0.04	1.86 ± 0.09
500	128	0.498 ± 0.013	3.67 ± 0.08	1.84 ± 0.09
1000	128	0.494 ± 0.005	4.25 ± 0.05	1.77 ± 0.08
500	256	0.473 ± 0.007	4.74 ± 0.11	1.56 ± 0.09
1000	256	0.485 ± 0.005	5.16 ± 0.08	1.64 ± 0.09
500	512	0.433 ± 0.007	5.19 ± 0.23	1.43 ± 0.09
1000	512	0.479 ± 0.012	5.81 ± 0.10	1.57 ± 0.09
500	1024	0.424 ± 0.006	5.76 ± 0.23	1.35 ± 0.06

Fig. 10. Dependence of the average radius R, average axial displacement Z (left axis) and average energy per ion E (right axis) on the scaled number of ions (given by ions × SF in Table 1) for clouds of 1000 ions.

and 10 ms of relaxation. The time evolution of macroscopic parameters sensitive to space-charge effects, such as the average ion radius R, the average axial displacement Z, and the per-ion energy E, was compared for complementary pairs of ion clouds (Table 1). Furthermore, the dependence of these parameters on the scaling factor, for clouds of 1000 ions, is shown in Fig. 10. As can be seen in Table 1, the average radial position of the ions in the cloud is typically different by a few percent only (i.e. well within error bars) for ion cloud pairs up to scaling factors (64,128), but diverging significantly for (128,256) and higher SFs. It is notable that the final R of all ion clouds of $10^3 - 1.28 \times 10^5$ ions is approximately equal, indicating that the centering efficiency is still not significantly hampered by the space-charge in this range. However, the axial displacement Z increases significantly for higher factors, due to more ions being "pushed out" axially when the cloud is "squeezed" radially by the excitation field forces. The average per-ion energy E at $t=290$ ms also agrees well for ion clouds scaled below factor 128. However, there is a trend of decreasing E with increasing total space-charge (see Fig. 10). The largest component of E stems from the residual energy of the quadrupolar excitations, indicating that ion clouds with lower total space-charge absorb more energy from the exciting field. This is most probably due to stronger shielding of the field by outer ions in cases of higher Coulomb scaling.

5.3. Buffer gas pressure estimation

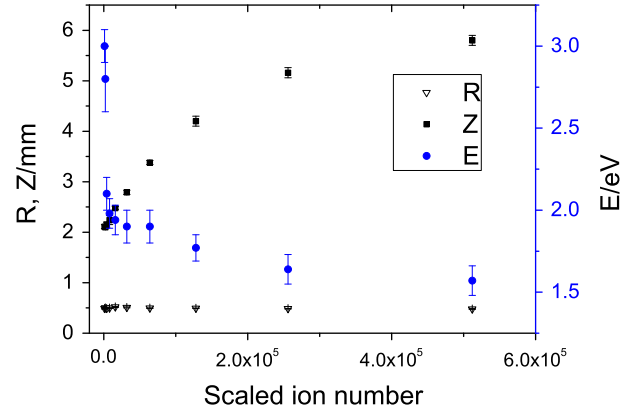The effect of buffer gas atoms on trapped ions with significantly higher energy than the buffer gas itself can be adequately modelled by viscous damping (Eq. (5)). This force will cause an exponential time-dependence of the ion velocity

$$v(t) = v(0)e^{-\delta t/m} \qquad (11)$$

where δ is given by Eq. (6). The time dependence of the total ion energy can then be written as

$$E_{TOT} = E_{Pot} + E_{kin}(0)e^{-2\delta t_{cool}/m} + E_{kin}(t_{cool} \longrightarrow \infty) \qquad (12)$$

where $E_{kin}(0)$ represents the initial kinetic energy of the ions, $E_{kin}(t_{cool} \longrightarrow \infty)$ the lower energy limit of the buffer gas cooling, i.e. thermalization with the buffer gas, and E_{Pot} the potential energy.

For different cooling times ranging from 20 to 200 ms the ion energy was measured by releasing the cloud from the CT into the DT, where a retardation barrier was varied from 0 to 10 V while other parameters were kept constant. In this way, the axial energy of the ion cloud was obtained as a function of the cooling time. This exponentially decaying cooling curve is shown in Fig. 11. It should be noted that this curve does not reach thermal equilibrium at a kinetic energy of about 0.025 eV. This is because a constant offset is produced when the quadrupolar trapping potential is switched to release the ions (see Fig. 4d), resulting in a total energy upon ejection of about 1.45 eV. The simulation was then fitted to the experimental cooling curves with buffer gas as the free parameter, resulting in a p_{CT} estimate. The small discrepancies between experimental and simulated data in Fig. 11 seen for the earliest cooling times are due to small differences in the not precisely known initial conditions for the real and simulated ion clouds. The buffer gas pressure was found to be $p_{CT} = 2.5(9) \times 10^{-5}$ mbar when the pressure at the gauge position was $p_{gauge} = 2 \times 10^{-2}$ mbar.

5.4. Simulation of sideband cooling resonances

The ion cloud was subjected to the same manipulations as in the corresponding experimental study: energetic ions were contained by a high end cap potential (~ 150 V), then cooled into a nested central quadrupolar potential well (~ 15 V) for up to 200 ms without excitations, and finally subjected to quadrupolar excitations for 80 ms at 3 V amplitude. The frequency was scanned over a few kHz from -2 kHz to 3.5 kHz around ν_c to determine the optimal cooling and centering frequency ν_{cool}, i.e. the central value and FWHM of the resonance curve. Fig. 12 (top) shows such a scan of ν_{cool} for 2000 ions scaled with a factor of 100, corresponding to a cloud of 2×10^5 ions in a buffer gas with $p_{CT} = 2.5 \times 10^{-5}$ mbar (see Section 5.2). A period of 100 ms of buffer gas cooling without excitations is followed by 120 ms of cooling and centering via
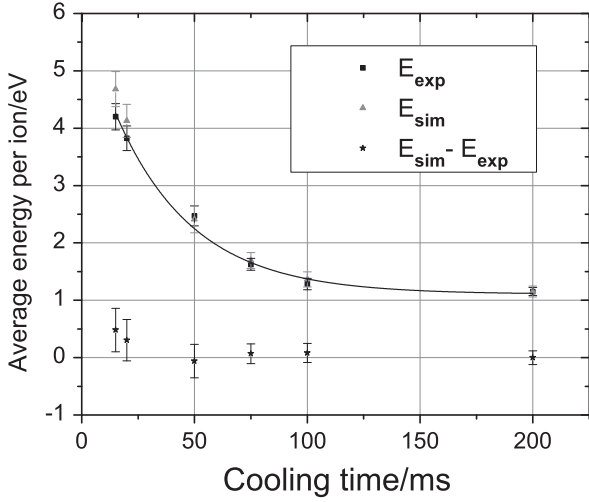
Fig. 11. Dependence of the mean axial energy per ion after ejection on the cooling time. Experimental data points E_{exp} (squares) are shown together with results from simulations E_{sim} (triangles). The line represents an exponential decay function fitted to the experimental data. The difference $E_{sim} - E_{exp}$ is also shown (stars).
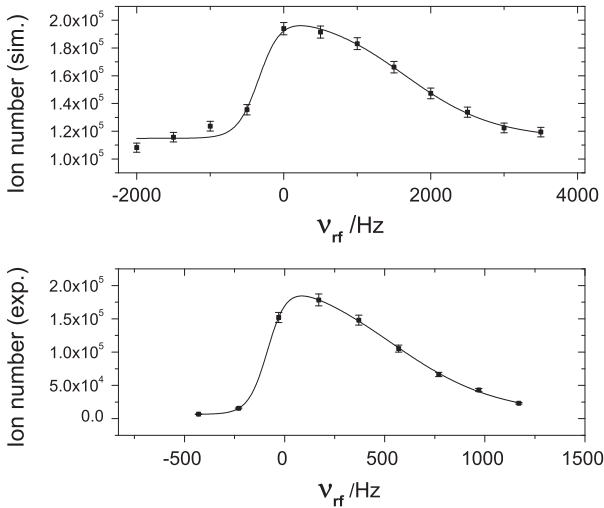

Fig. 12. Experimental scan of the cooling frequency ν_{cool} shift (bottom) and a simulated scan with matching parameters (top). Zero of the horizontal axis corresponds to ν_c. The empirical fitted function is an asymmetric double sigmoid.

Fig. 13. Comparison of measured and simulated relative shifts of the cooling frequency ν_{cool}.
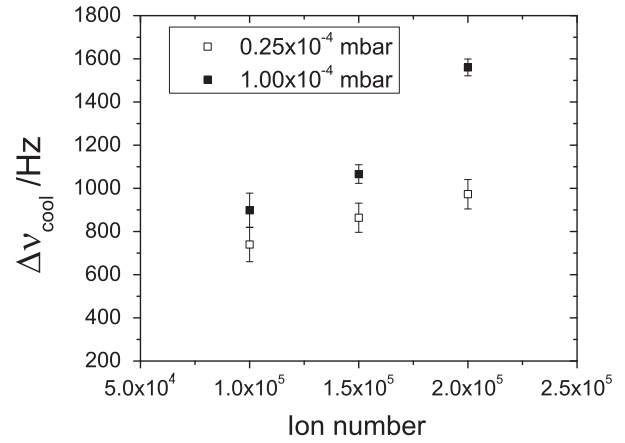
Fig. 14. Comparison of simulated ν_{cool} shifts for different buffer gas pressures in the CT.

quadrupolar excitations with 3 V amplitude. The ions were considered to be centered if the radius of their motion was smaller than the diaphragm radius. Fig. 12 (bottom) shows an experimental scan with matching parameters. Both resonances are asymmetric in shape, with the number of ions rising sharply at the lower end of ν_{rf} and decreasing more gradually at the high-frequency side. This behavior is in agreement with results of the mean-field model of the space-charge frequency shifts from [43]. The optimal cooling frequency, ν_{cool}, is accurately reproduced by simulations. However, the FWHMs of the experimental resonance peaks are reproduced less well and there is an offset of the baseline due to incomplete knowledge of the initial position of the ion cloud in the trap.

Fig. 13 compares measured and simulated relative shifts of the optimal cooling frequency ν_{cool} for experimental data and simulated ion clouds in identical conditions as described previously. The offset corresponding to zero ions was extrapolated and used as a reference for experimental and simulation data. The simulation is in good agreement with experimental data, especially in
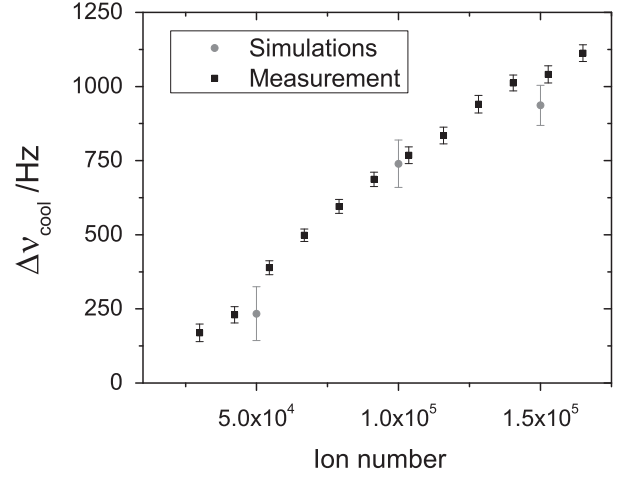
view of the uncertainties in the estimation of p_{CT} and in our understanding of the initial conditions of the ion cloud.

Fig. 14 shows a simulation of the difference in frequency shifts $\Delta\nu_{cool}$ between $p_{CT} = 2.5 \times 10^{-5}$ mbar and $p_{CT} = 1.0 \times 10^{-4}$ mbar, with all other simulation parameters kept constant. The ν_{cool} resonance frequency of the ion cloud increases for higher values of p_{CT}, being in qualitative agreement with experimental data as shown in Fig. 6. It should be noted though that quantitative comparison of data in Figs. 6 and 14 is not possible, since the estimation (see Section 5.3) for p_{CT} is not available in these cases.

Figs. 15 and 16 show the simulated dependence of the ν_{cool} peak FWHM on p_{CT} and on space-charge, i.e. the number of ions. The FWHM is increasing with p_{CT}, in qualitative agreement with experimental data. However, an accurate quantitative comparison of the effect of the space-charge and p_{CT} on the FWHM is limited by the precision and availability of the experimental value for p_{CT}. Furthermore, while Coulomb scaling can consistently reproduce the space-charge conditions of a large ion cloud ($\sim 2 \times 10^5$ ions), the cumulative interaction with the Helium buffer gas in the case presented here amounts only to a cloud of 2×10^3 ions. This mismatch of simulated and experimental conditions is identified as a possible reason for the discrepancy between the simulated and experimental FWHM that can be seen in Fig. 16. The simulation is seen to significantly underestimate the FWHM for the experimentally estimated $p_{CT} = 2.5 \times 10^{-5}$ mbar. For the higher simulated pressure of 1×10^{-4} mbar the FWHM behavior is similar to the case of lower space charge values, although sharply rising
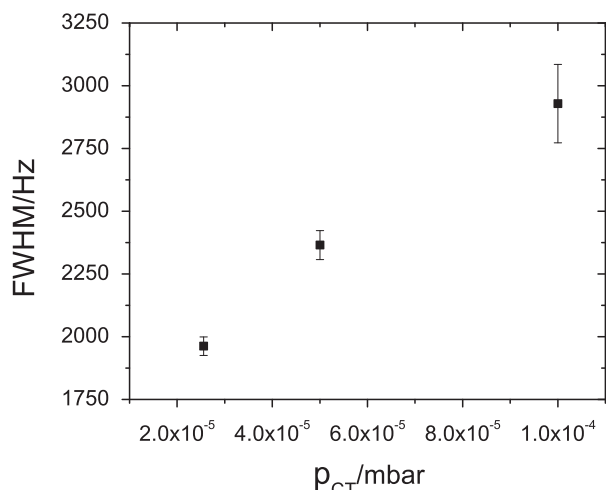
Fig. 15. Dependence of the FWHM of the simulated ν_{cool} on p_{CT} for a cloud of 10^5 ions.
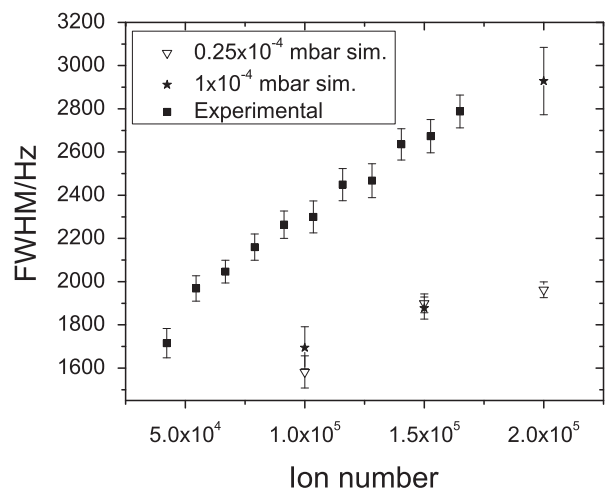

Fig. 16. Comparison of simulated ν_{cool} FWHM dependence on the amount of ions for different buffer gas pressures with experimental data.

at about 2×10^5 ions. Since the simulation of $\sim 10^5$ ions without Coulomb scaling with current GPU technology is not feasible because of computation time limitations, these effects will require improvements in simulation speed for accurate predictions under the given experimental conditions.

6. Summary and outlook

Systematic effects related to space-charge present challenges for successful operation of the WITCH system as well as other existing or planned Penning traps. They have been investigated both experimentally and numerically in this work.

The buffer gas pressure inside the Cooler Trap was estimated through measurement of the ion cloud cooling rate and comparison with simulations. Since pressure gauges cannot be operated in the close vicinity of a Penning trap, this approach provides a useful, albeit less accurate alternative.

Off-center magnetron motion of the entire ion cloud was observed experimentally in the WITCH Penning traps. It was found to be of significant importance as a systematic effect in the WITCH on-line experimental data. Its eigenfrequency ν_- was studied under different space-charge conditions. It was found that it rises proportionally with the number of ions, as is expected from

theory. This result provides an essential correction to the on-line retardation spectrum data of WITCH [44].

The influence of space-charge on the eigenfrequency ν_{cool} has been investigated. $^{39}K^+$ ions were subjected to the buffer gas cooling technique and its effectiveness in different space-charge and buffer gas conditions was measured. It was found that space-charge and buffer gas both independently cause the increase of center frequencies and FWHM's of the cooling resonances. The results are in agreement with experimental investigations of these effects conducted in another high-capacity gas-filled Penning trap (REXTRAP) [1,12]. The properties of the ν_{cool} peaks i.e. their center frequency and FWHM in specific experimental conditions are of special interest for improving the understanding of high-capacity Penning traps and their operation as mass separators.

The Simbuca software for *ab initio* simulation of ion cloud dynamics in particle traps was benchmarked against experimental results, successfully simulating complex dynamics of a large ion cloud in a buffer-gas filled Penning trap modelled using realistic field maps. Shifts of ν_{cool} peaks under increasing space-charge were accurately reproduced for different experimental conditions, while other effects such as the influence of space-charge and of the buffer gas pressure in the trap on the FWHM were reproduced qualitatively. With the help of a novel simulation method on GPU's that allows significantly higher simulated number of ions, these results expand on earlier computational studies of space-charge and buffer gas effects on cooling resonances in Penning traps [18,45].

These results establish Simbuca as a promising tool for Penning trap optimization and design. The study presented here, i.e. investigating the effect of space-charge on ion dynamics, further contributes toward the effort to understand fundamental properties of Penning traps and to increase their application domain.

References

[1] F. Ames, et al., Nuclear Instruments and Methods in Physics Research Section A: Accelerators, Spectrometers, Detectors and Associated Equipment 538 (2005) 17.
[2] K. Blaum, Physics Reports 425 (2006) 1.
[3] M. Kowalska, et al., European Physical Journal A 42 (2009) 351.
[4] C. Amole, et al., Nuclear Instruments and Methods in Physics Research Section A: Accelerators, Spectrometers, Detectors and Associated Equipment 735 (2014) 319.
[5] J.N. Tan, et al., Physical Review Letters 75 (1995) 4198.
[6] S. Van Gorp, et al., Physical Review C 90 (2014) 025502.
[7] M. Beck, et al., Nuclear Instruments and Methods in Physics Research Section A: Accelerators, Spectrometers, Detectors and Associated Equipment 503 (2003) 267.
[8] V. Kozlov, et al., Nuclear Instruments and Methods in Physics Research Section B: Beam Interactions with Materials and Atoms 266 (2008) 4515.
[9] N. Severijns, O. Naviliat-Cuncic, Annual Review Of Nuclear And Particle Science 61 (2011) 23.
[10] M. Beck, et al., European Physical Journal A 47 (3).
[11] M. Mehlman, et al., Nuclear Instruments and Methods in Physics Research Section A: Accelerators, Spectrometers, Detectors and Associated Equipment 712 (0) (2013) 9.
[12] A. Gustafsson, et al., Nuclear Instruments and Methods in Physics Research Section A: Accelerators, Spectrometers, Detectors and Associated Equipment 626 (2011) 8.

[13] S. Van Gorp, et al., Nuclear Instruments and Methods in Physics Research Section A: Accelerators, Spectrometers, Detectors and Associated Equipment 638 (2011) 192.
[14] R. Wolf, et al., International Journal of Mass Spectrometry 349–350 (2013) 123.
[15] A. Herlert, et al., Hyperfine Interactions 199 (2011) 211.
[16] D. Voulot, et al., Nuclear Instruments and Methods in Physics Research Section B: Beam Interactions with Materials and Atoms 266 (2008) 4103.
[17] P. Ascher, et al., in: EPJ Web of Conferences, vol. 66, 2014, p. 11002.
[18] D. Beck, et al., Hyperfine Interactions 132 (1–4) (2001) 469.
[19] S. Coeck, et al., Nuclear Instruments and Methods in Physics Research Section A: Accelerators, Spectrometers, Detectors and Associated Equipment 572 (2007) 585.
[20] G. Savard, et al., Physics Letters A 158 (1991) 247.
[21] M. Mukherjee, et al., European Physical Journal A 35 (2008) 1.
[22] M. Block, et al., European Physical Journal A 25 (2005) 49.
[23] A.J. Peurrung, et al., International Journal of Mass Spectrometry 157 (1996) 80.
[24] D.F.A. Winters, et al., Journal of Physics B: Atomic, Molecular and Optical Physics 39 (2006) 3131.
[25] J. Jeffries, et al., International Journal of Mass Spectrometry 54 (1983) 169.
[26] A. Picard, et al., Nuclear Instruments and Methods in Physics Research Section B: Beam Interactions with Materials and Atoms 63 (1992) 345.
[27] E. Liénard, et al., Nuclear Instruments and Methods in Physics Research Section A: Accelerators, Spectrometers, Detectors and Associated Equipment 551 (2-3) (2005) 375.
[28] S. Coeck, et al., Nuclear Instruments and Methods in Physics Research Section A: Accelerators, Spectrometers, Detectors and Associated Equipment 557 (2006) 516.
[29] E. Traykov, et al., Nuclear Instruments and Methods in Physics Research Section A: Accelerators, Spectrometers, Detectors and Associated Equipment 648 (2011) 1.
[30] V.Y. Kozlov, et al., International Journal of Mass Spectrometry 251 (2006) 159.
[31] S. Van Gorp, Search for physics beyond the standard electroweak model with the WITCH experiment. (Ph.D. thesis), KU Leuven, (2012) ⟨https://fys.kuleuven.be/iks/wi/WITCH/files/phds/thesis–simonvangorp.pdf⟩.
[32] M. Tandecki, et al., Nuclear Instruments and Methods in Physics Research Section A: Accelerators, Spectrometers, Detectors and Associated Equipment 629 (2011) 396.
[33] P. Friedag Setup and calibration of a position sensitive microchannel plate detector and analysis of a test run optimizing the WITCH experiment, (Ph.D. thesis), Westfälischen Wilhelms-Universität Münster, (2013) ⟨http://repositorium.uni-muenster.de/document/miami/627d5ad1-6043-417b-94ba-5c87309-bc2bd/diss_friedag.pdf⟩.
[34] K. Valerius Spectrometer-related background processes and their suppression in the KATRIN experiment (Ph.D. thesis), Westfälischen Wilhelms-Universität Münster, 2009, ⟨http://repositorium.uni-muenster.de/document/miami/93137705-73f4-404a-a438-09d487cbff63/diss_valerius.pdf⟩.
[35] M. Tandecki (Ph.D. thesis), Katholieke Universiteit Leuven, (2011) ⟨https://fys.kuleuven.be/iks/wi/files/final–version–thesis–michael–tandecki.pdf⟩.
[36] E. Wursten Searching for Exotic Weak Currents with the WITCH Experiment, (M.Sc. thesis), KU Leuven, (2013) ⟨https://fys.kuleuven.be/iks/wi/files/Elise-Thesis-Master.pdf⟩.
[37] J. Barnes, P. Hut, Nature 324 (1986) 446.
[38] V. Rokhlin, Journal of Computational Physics 60 (1985) 187.
[39] T. Hamada, T. Iitaka, http://arxiv.org/abs/astro-ph/0703100.
[40] M. Petersson, A Monte Carlo method for the simulation of buffer-gas cooling inside a radio frequency quadrupole (Ph.D. thesis), Linkoping University, 2002.
[41] Dormand Prince, Journal of Computational and Applied Mathematics 6 (1) (1980) 19.
[42] COMSOL Multiphysics Software, ⟨http://www.comsol.com⟩.
[43] S. Sturm Implementation of a mass separation method in the Penning trap REXTRAP and investigation of space-charge related phenomena, 2007 (M.Sc. thesis), University of Heidelberg.
[44] T. Porobić (Ph.D. thesis), KU Leuven, in preparation.
[45] S. Coeck, et al., Nuclear Instruments and Methods in Physics Research Section A: Accelerators, Spectrometers, Detectors and Associated Equipment 574 (2007) 370.